Department of Physics and Astronomy
Heidelberg University

Bachelor thesis in physics
submitted by

Robert Wright

born in Heidelberg, Germany

2021

Imaging Water-Sided Oxygen Concentration Fields at the Wind-Driven Air-Water Interface by Fluorescence Quenching

This bachelor thesis has been carried out by Robert Wright at the
Institute of Environmental Physics (IUP) in Heidelberg
under the supervision of

Prof. Dr. Bernd Jähne

Abstract

In this study, an imaging method to resolve horizontal oxygen concentration fields is presented. The technique is based on the transformation of a concentration gradient into fluorescence intensity. A water-soluble ruthenium complex indicator is quenched by oxygen. The boundary layer imaging setup has been mounted on a small annular wind-wave tank at the IUP Heidelberg. Measurement series have been performed for three different indicator concentrations (0.03 mmol L^{-1}, 0.07 mmol L^{-1} and 0.11 mmol L^{-1}) at wind speeds ranging from 2 m s^{-1} to 7 m s^{-1}. The recorded images clearly show gas transport footprints, which are qualitatively discussed. The mean brightness of image sequences is quantitatively analysed. The oxygen quenching method has been implemented, and the setup is ready for further use.

Zusammenfassung

In dieser Arbeit wird eine bildgebende Messtechnik zur Bestimmung von horizontalen Sauerstoffkonzentrationsfeldern angewendet. Die Methode basiert auf der Umwandlung von Konzentrationsunterschieden des gelösten Gases in fluoreszierende Strahlung. Ein wasserlöslicher Ruthenium-Komplex fungiert als Indikator und wird durch Sauerstoff “gequencht”. Der Aufbau zum Aufnehmen der Grenzschicht ist am kleinen ringförmigen Windwellenkanal des IUP Heidelberg installiert. Es wurden Messreihen für drei verschiedene Konzentrationen des Indikators (0,03 mmol L^{-1}, 0,07 mmol L^{-1} und 0,11 mmol L^{-1}) bei Windgeschwindigkeiten im Bereich von 2 m s^{-1} bis 7 m s^{-1} durchgeführt. Die aufgenommenen Bilder zeigen deutliche Spuren des Gastransports durch die Grenzschicht, welche qualitativ diskutiert werden. Die mittlere Helligkeit der Bildsequenzen wird quantitativ analysiert. Die Methode der Fluoreszenzlöschung mittels Sauerstoff wurde implementiert und der Versuchsaufbau ist für die weitere Verwendung eingerichtet.

Contents

1 Introduction

The exchange of environmentally relevant trace gases, especially between ocean and atmosphere, plays a key role for the understanding of the past, current and future climate [IPCC 2013]. However, it is yet unknown which physical model gives the best description of the complex gas transport processes at the air-water interface. Generally speaking, multiple environmental variables influence the exchange of gases at the ocean surface. Wind, blowing over the water surface, accelerates the gas transfer velocity. Likewise, gravity and capillary waves, surface-active materials and bubble entrainment affect the gas transport. The measurement of vertical concentration profiles in the mass boundary layer at the air-water interface aims at verifying theoretical considerations with experimental data [Arnold 2015; Friedl 2013]. Since the water-sided mass boundary layer is in the order of 20 µm to 200 µm [Jähne et al. 1987], such methods require a high spatial resolution. On top, high temporal resolution is necessary to detect the water surface in vertical profiles.

In order to measure near-surface processes enhancing the gas exchange (e.g., Langmuir circulation, see section 2.2.2), it is desirable to image the water surface horizontally. Kräuter [2015] used a pH-sensitive dye to transform gas concentrations into fluorescence intensity. Such a transformation can also be reached by quenching a luminescent indicator; the so-called (oxygen) quenching method is implemented in this study. Therefore, an annular wind-wave tank at the IUP Heidelberg is equipped with new measuring devices and a boundary layer imaging setup, then, for the first time, horizontal water-sided oxygen concentration fields are resolved through dynamic quenching.

2 Theoretical Background

This chapter is intended to give the reader a broad understanding of the most important theoretical considerations. It is divided into three parts, section 2.1 explains the gas transport across the air-water interface, section 2.2 discusses turbulent processes visible at the water surface and section 2.3 introduces luminescence theory. The structure of this chapter is based on Friedl [2013] and Kräuter [2015].

2.1 Gas Transport

Gas transport is driven by either random or direct motion. Molecular diffusion and turbulent flow are random transport processes, that compensate for disequilibriums of the fluid. Generally speaking, turbulent transport is more efficient than molecular diffusion, however, close to the air-water interface, the latter dominates. On the other hand, there is advection, which is a direct motion driven by the mean bulk velocity of a fluid. This section introduces the gas transport mechanisms, regarding the processes at the interface separately in section 2.1.3.

2.1.1 Molecular Diffusion

Brownian motion describes the random fluctuations of particles due to their thermal energy. The molecules (or atoms) move around freely, until elastically colliding with other

molecules and moving in new directions, which are uncorrelated to the previous ones. This stochastic movement can be described by the random walk model, and is the driving mechanism of molecular diffusion. The result of which is a net flux of molecules from regions of high concentration to regions of low concentration, gradually mixing a medium until the particle distribution is uniform.

Mathematically, Fick [1855] suggested a relation between the concentration flux density $\boldsymbol{j}_c$ and the concentration gradient ∇c as follows:

$$\boldsymbol{j}_c = -D\nabla c, \tag{2.1}$$

which is nowadays referred to as **Fick's first law**. The proportionality constant D is referred to as **diffusion coefficient** and defined as

$$D = \frac{1}{3}ul, \tag{2.2}$$

with the particles' mean thermal velocity u and mean free path l. In analogy to eq. (2.1), **Newton's law** of viscosity describes the flux of momentum

$$\boldsymbol{j}_m = -\nu\nabla(\rho u), \tag{2.3}$$

with the kinematic viscosity ν, the fluid density ρ, and the mean velocity u. Inserting eq. (2.1) into the continuity equation, i.e., assuming mass conservation in absence of any chemical reactions, yields the temporal change in concentration

$$\frac{\partial c}{\partial t} = D\Delta c, \tag{2.4}$$

which is known as **Fick's second law**. Likewise, diffusion equations for heat and momentum transfer can be formulated, please refer to Kräuter [2015].

2.1.2 Turbulence

Turbulent flow is driven by random fluctuations of the fluid's velocity field. Commonly, turbulence is described with the concept of eddies at various length scales. Such eddies are characterized by swirling motion. Turbulent energy is transferred from large to small eddies, until at very small scales in the order of millimetres, this energy cascade is dissipated by molecular friction and converted to thermal energy. Far away from the air-water interface, the length scale of turbulent eddies is much larger than the mean free path of particles, hence, turbulent transport is more efficient than molecular diffusion.

In order to predict the flow behaviour (laminar or turbulent) of a fluid, the dimensionless **Reynolds number**

$$\mathrm{Re} = \frac{ul}{\nu} \tag{2.5}$$

is introduced, where u is the mean velocity, ν the kinematic viscosity of the medium, and l the characteristic length [Stokes 1850]. Equation (2.5) represents the ratio of inertial to viscous forces, i.e., at low Reynolds numbers laminar (sheet-like) flow dominates, whereas at high numbers above a critical threshold, the flow immediately tends to be turbulent.

While molecular diffusion is limited to small scales and macroscopically described by Fick's first law (eq. (2.1)), turbulent eddies occur on all scales, creating a very complex phenomenon. Turbulent flow is described by separating the expectation value (here, temporal mean, denoted by dash) of a quantity from its fluctuations (denoted by prime), a mathematical technique called **Reynolds decomposition**, resulting in

$$c = \overline{c} + c', \tag{2.6}$$

$$\boldsymbol{u} = \overline{\boldsymbol{u}} + \boldsymbol{u}'. \tag{2.7}$$

To simplify things, only a concentration gradient in z-direction is considered in the following. Inserting eqs. (2.6) and (2.7) into the equation of concentration flux $j_{c,z} = u_z c$, and time-averaging the result, yields

$$j_{c,z} = \overline{cu_z} + \overline{c'u'_z}, \tag{2.8}$$

considering that $\overline{c'} = \overline{u'} = 0$, because the mean of the fluctuating component is equal to zero. The first term of eq. (2.8) describes the advection of the mean concentration with the mean flow, the second term the turbulent flux. The **turbulent diffusion coefficient** K can be defined as

$$K(z) := -\frac{\overline{c'u'_z}}{\frac{\partial \overline{c}}{\partial z}}, \tag{2.9}$$

which allows re-writing the turbulent flux term of eq. (2.8) as

$$j_{c,z} = -K(z)\frac{\partial \overline{c}}{\partial z}, \tag{2.10}$$

yielding an analogy to the mathematical description of molecular diffusion.

Again, a turbulent flux density, also referred to as Reynolds stress, can be derived for momentum

$$j_{m,turb} = \rho u_\star^2, \tag{2.11}$$

with the friction velocity

$$u_\star = \sqrt{\overline{u'_i u'_j}}, \tag{2.12}$$

where Cartesian vector index notation is used for the velocity field. Note, that eq. (2.11) is only applicable in the fully turbulent flow regime.

2.1.3 Boundary Layers

Regions, where a variable of a system changes tremendously, are generally referred to as boundary layers. The area of such change is the transition zone, whereas, the interface of the boundary layer shows an abrupt discontinuity (e.g., water surface). In the water bulk, turbulent transport is more effective than molecular diffusion, i.e., $K \gg D$. However, as already noted, in boundary layers at the air-water-interface, molecular diffusion dominates ($K < D$). The size of the turbulent eddies scales with the distance to the interface, ultimately leading to $K(0) = 0$ at the water surface. Since random motion is a slow transport process, the boundary layer acts as a bottleneck of the exchange.

Put together, eqs. (2.1) and (2.10) summarize the effects of molecular diffusion and turbulence, leading to

$$j_c = -\left(K(z) + D\right) \frac{\partial c}{\partial z}, \tag{2.13}$$

describing the concentration flux in z-direction. For a stationary concentration profile, the flux has to be constant over depth due to mass conservation. Likewise, the molecular diffusion coefficient D is independent of z. The length scale of eddies increases with greater distance from the air-sea interface, thus, leading to a larger turbulent diffusion coefficient K. Accordingly, the concentration gradient increases with decreasing distance to the water surface. Figure 2.1 schematically depicts a typical vertical profile of concentration. The **boundary layer thickness** $z_\star$ corresponds to the depth, at which the molecular and turbulent diffusion coefficients are of the same order. It is defined as the ratio of the concentration difference between surface and bulk, and the concentration gradient at the surface

$$z_\star = \frac{\Delta c}{\frac{\partial c}{\partial z}\big|_{z=0}}. \tag{2.14}$$

In water, typical values of $z_\star$ are of the order of 100 µm [Jähne et al. 1987].

2.2 Turbulent Processes

2.2.1 Shear Stress

If wind blows over a water surface, it transports momentum across the interface. The shear stress τ is force F per unit area A

$$\tau = \frac{F}{A}, \tag{2.15}$$

and acts coplanar to the surface. The corresponding shear flow is wall-bounded. Close to the water surface, the Reynolds stress vanishes, and the flow is laminar. The shear stress is equal to the momentum flux, hence, eq. (2.3) can be re-written as

$$\tau = \nu\rho\frac{\partial u}{\partial z}. \tag{2.16}$$

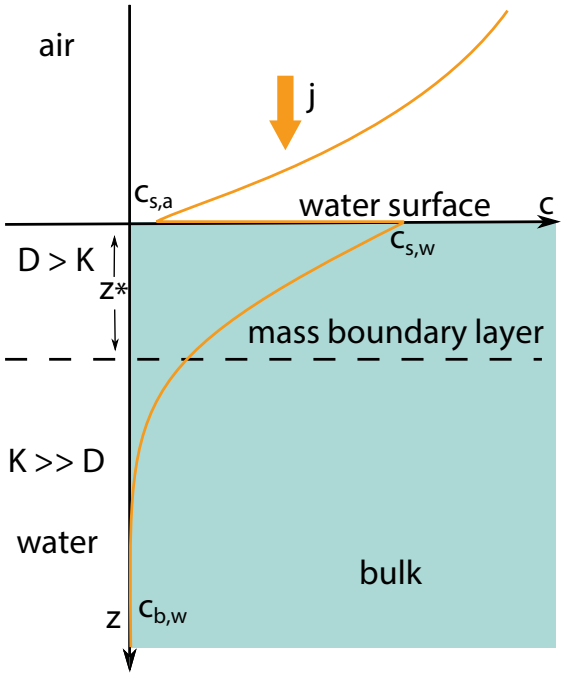

Figure 2.1: Vertical concentration profile near the air-water interface of invasion experiment. The gas solubility $\alpha > 1$ determines the magnitude of the concentration discontinuity at the water surface ($c_{s,w} = \alpha \cdot c_{s,a}$). The concentration is plotted on the x-axis, the water depth on the y-axis. The thickness of the mass boundary layer is indicated by a dashed line. From Kräuter [2015].

Here, the negative sign is omitted for conventional reasons and the velocity gradient is in z-direction only. Integrating eq. (2.16) yields a linear wind profile

$$u(z) \propto z. \tag{2.17}$$

This region is known as the viscous sublayer, at the water-side it is much larger than the mass boundary layer, while at the air-side the thickness of both layers is approximately the same. In the fully turbulent flow region, the shear stress is equal to the Reynolds stress, introduced in eq. (2.11), as the viscous contribution can be neglected. The wind profile has a logarithmic form

$$u(z) = \frac{u_\star}{\kappa} \cdot \ln \frac{z}{z_0}, \tag{2.18}$$

with the universal Von Kármán constant κ and the roughness parameter z_0. The velocity profile is described by the **law of the wall**, a derivation can be found in Roedel and Wagner [2011]. In the outer layer or wake part, no theory has been developed to describe the wind profile, however, experiments indicate self-similarities of the profile in this region [Hinze 1975].

2.2.2 Langmuir Circulation

Langmuir cells are described as a series of counter-rotating vortices at the water surface, with rotational axes parallel to the wind. Due to the alternating signs of the vortices, regions of divergence and convergence are created. Langmuir [1938] discovered the phenomenon after observing multiple streaks of seaweed in the Sargasso Sea. Naturally, in convergence zones, algae, bubbles or foam aggregate. Such bands are also called windrows and can be found, under the appropriate conditions, at the surface of lakes, rivers and oceans. Figure 2.2 depicts a schematic drawing of the driving mechanism and a photograph of the resulting patterns at the water surface.

The Stokes drift is the net drift velocity in the direction of wave propagation, however, a fluid parcel also moves up and down in the waves, causing it to progress in spirals. The Craik-Leibovich theory states that the vorticity of the flow near the surface is stretched and

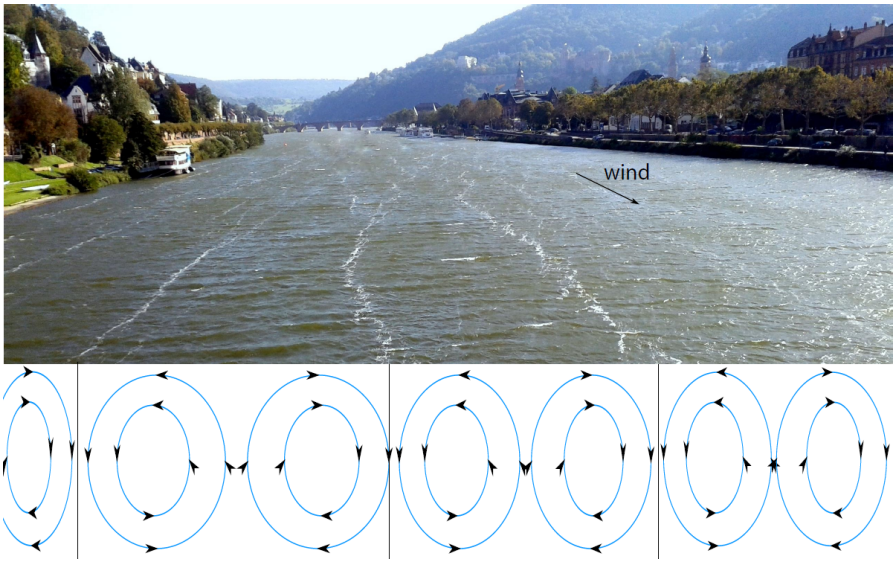

Figure 2.2: Windrows of accumulated foam on the river Neckar in Heidelberg are due to the Langmuir circulation. The arrow in the photograph indicates wind direction. From Kräuter [2015].

tilted due to the Stokes drift. The production of vorticity in the upper layers is balanced by downward turbulent diffusion, initiating Langmuir circulation. The rotating cells enhance the vertical mixing from the water surface to the bulk, thus, having a great influence on gas exchange processes. Veron and Melville [2001] stated that gas transfer velocities are increased by a factor of 1.7 to 2 at the onset of Langmuir circulation, making the process one of the main contributors to air-water gas transport at low wind speeds.

2.3 Luminescence

Luminescence is the spontaneous emission of light and can be classified depending on the form of excitation. If initiated by photoexcitation, i.e., if photons excite electrons to a higher energy level in an atom, the resulting light emission is referred to as photoluminescence, which is deployed in this study. Likewise, chemo-, thermo-, and electroluminescence describe an excitation by chemical reactions, thermal energy and voltage differences, respectively.

2.3.1 Fluorescence & Phosphorescence

Luminescent processes can be divided into two categories. The Jablonski diagram in fig. 2.3 displays both types of luminescence and helps to understand the following remarks.

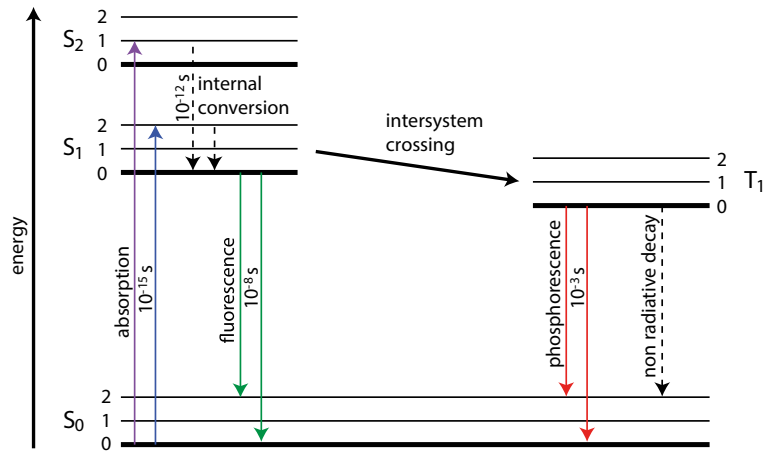

Figure 2.3: Jablonski diagram depicting luminescent processes: Light emission from relaxation of a singlet state (S) or a triplet state (T) to the ground state is called fluorescence or phosphorescence, respectively. Integers denote the vibrational energy levels an individual state splits into. The decay processes are indicated by arrows, their typical lifetime is given. As an example, two possible decaying paths for fluorescence and phosphorescence are shown. Modified from Friedl [2013].

First, fluorescence occurs when an excited molecule (or atom) relaxes into a state of lower energy through emission of a photon without a change in electron spin. The ground state of the molecule is typically a singlet state, denoted as S_0. Absorbing a photon leads to an excited state S_n of the same multiplicity[1] as the ground state, with $n > 0$. The absorption is quasi-instantaneous, in the order of 10^{-15} s. In a singlet state, the electron spins are paired, i.e., the spin of the excited electron still has an opposite sign than that of its counterpart at ground state. In solution, states with $n > 1$ rapidly relax to the lowest vibrational level

[1]The multiplicity $2S + 1$ describes the number of degenerate spin states, where S is the total spin quantum number.

of the first excited state S_1 through non-radiative processes, such as internal conversion. This decay path has a lifetime of about 10^{-12} s, which is much shorter than the lifetime of fluorescence, being in the order of 10^{-8} s. Therefore, the fluorescent decay occurs from the lowest vibrational level of the first singlet excited state S_1 to any vibrational level of the ground state S_0. The energy of the fluorescence photons is lower than the initial energy used to generate the excited state.

Second, in the case of phosphorescence, the excited electron undergoes intersystem crossing into an energy state of higher spin multiplicity, usually a triplet state, here, denoted as the first excited triplet state T_1. Hence, in phosphorescent molecules, the decay path of intersystem crossing has to be faster than that of fluorescence. In a triplet state, the spin of the electron is not paired with that of the electron at ground state any more. Hence, the excited electron undergoes spin conversion and becomes trapped in the triplet state T_1, with only "forbidden" transitions available to return to the lower energy singlet state. The relaxation to S_0, i.e., the phosphorescent decay, thus progresses at significantly slower time scales of 10^{-3} s.
Aside from fluorescence and phosphorescence, an excited state can also decay to the ground state S_0 without emitting radiation, e.g., by collisional quenching.

2.3.2 Quenching

Quenching prevents the light emission of a luminescent molecule. This interaction can either be static or dynamic. Static quenching occurs when the quencher (the molecule provoking quenching effects) and the luminescent molecule form a non-fluorescent complex in the ground state, i.e., before excitation. Dynamic or collisional quenching leads to a non-radiative decay of the excited luminescent molecule and is caused by different mechanisms, e.g., Förster resonance energy transfer and Dexter electron transfer. Generally speaking, the quencher must diffuse to the luminescent molecule during the lifetime of the excited state and, upon contact, dynamic quenching processes transfer the energy of the excited electron to the quencher. The luminescent molecule returns to the ground state without emission of a photon. Molecular oxygen (O_2) is an extremely efficient quencher.

3 Methods

This chapter gives a short overview on how oxygen profiles can be resolved in the following, and introduces in section 3.2 the specific indicator, i.e., the luminescent molecule, used for the boundary layer imaging.

3.1 Oxygen Concentration Imaging

Gas concentrations in the water-sided mass boundary layer can be imaged by two non-intrusive methods. First, the concentration gradient of a dissolved gas can be transformed into a step function of pH, which in turn is visualized with the help of a fluorescent pH-indicator, as, e.g., applied by Kräuter [2015]. Second, in the quenching method, the trace gas acts as a quencher, which decreases the light emission of a luminescent indicator. Both methods are laser-induced fluorescence (LIF) techniques, in which a light source, such as a laser or light-emitting diode, excites an indicator, which in turn emits luminescent light detectable with a camera.

In this study, the quenching method is used to record water-sided oxygen concentrations. It was first presented by Wolff et al. [1991]. Using this technique, Arnold [2015] and Friedl [2013] recorded vertical oxygen concentration profiles parallel and transverse to the wind direction, respectively. The Stern-Volmer equation, generalized by Friedl [2013], describes how the photon flux decreases with increasing oxygen concentration.

3.2 Ruthenium Complex Indicator

The water-soluble complex $[Ru(dpp(SO_3Na)_2)_3]Cl_2$ is used as a luminescent indicator, typified by the expression [metal(ligand)]. In the following, it is simply referred to as Ruthenium (Ru) complex. Three ligands $dpp(SO_3Na)_2$ are attached to the metal Ru; the ligand is a disulfonated derivative of 4,7-diphenyl-1,10-phenantroline (dpp). Based on the oxygen probe $[Ru(dpp)_3]Cl_2$, Castellano and Lakowicz [1998] first synthesized the Ru complex in its current form, which is now widely used as an oxygen indicator. The authors reported a fluorescence lifetime of the unquenched Ru complex of 3.7 µs. A schematic drawing of the indicator is provided in fig. 3.1, while the absorption and emission spectra are displayed in fig. 3.2.

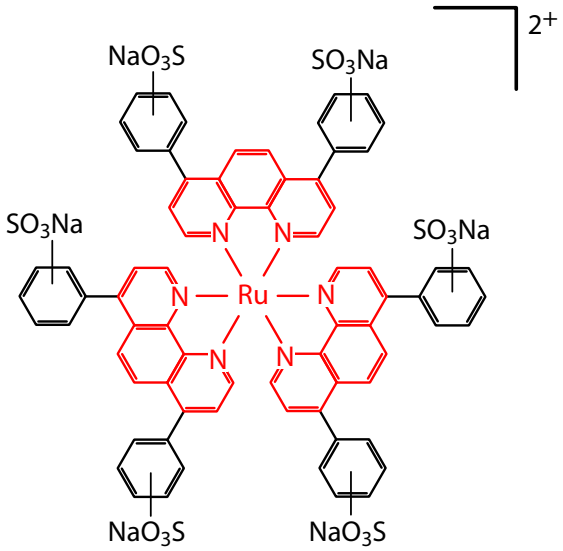

Figure 3.1: Schematic drawing of the water-soluble metal-ligand complex $[Ru(dpp(SO_3Na)_2)_3]Cl_2$. The metal Ru is at the centre, surrounded by the ligand 4,7-diphenyl-1,10-phenantroline. The SO_3Na groups ensure water solubility. From Friedl [2013].

The Ru complex is excited by metal-to-ligand charge transfer (MLCT). The outermost shell of the Ru has five d-orbital energy levels, which are separated into three lower (d_l) and five higher (d_h) states with an energy gap of Δ. The transition from the d_l-orbital to the d_h-orbital is quantum mechanically "forbidden", on top, an excitation of the d_h-orbital would

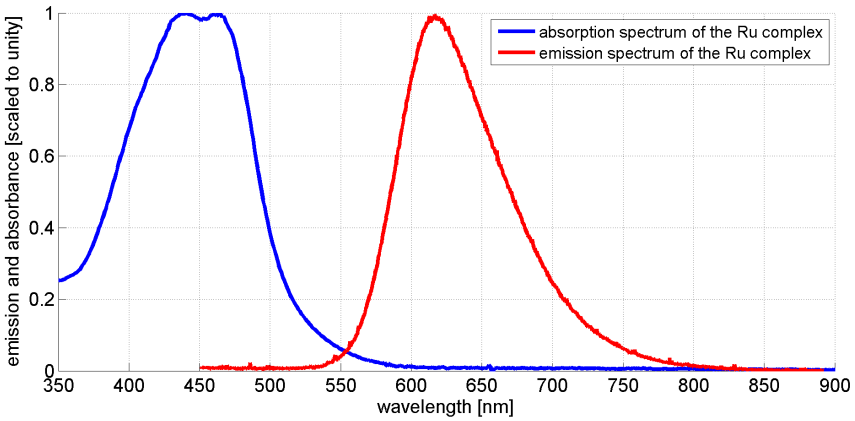

Figure 3.2: The absorption and emission spectra of the Ru complex scaled to unity. The maximum absorbance ranges from 440 nm to 465 nm, the maximum emission wavelength is at about 616 nm. The self-absorption of the Ru complex can be neglected, because of the spectral separation of absorbance and emittance. From Friedl [2013].

be quenched with a high probability. However, an electron can be excited to the singlet MLCT state, as indicated in fig. 3.3, next, intersystem crossing to the triplet MLCT state occurs in less than 300 fs [Lakowicz 2006]. From the triplet state, the excited complex decays by phosphorescent emission. Due to spin-orbit coupling between the ligand and the transition metal, the decay time is short compared to typical phosphorescent molecules.

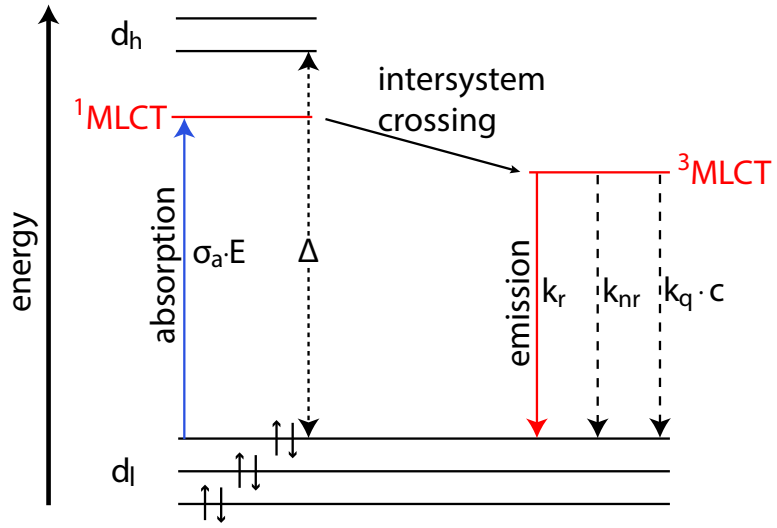

Figure 3.3: Jablonski diagram illustrating the metal-to-ligand charge transfer in the Ru complex. The low and high d-orbitals are separated by the energy gap Δ, and labelled with the superscript l and h, respectively. The six valence electrons of the outer orbit are indicated as pairs of arrows, pointing in the direction of spin. The product of absorption cross-section σ_a and photon irradiance E describes the probability of an absorption process to the singlet ^{1}MLCT state. The transition from the triplet ^{3}MLCT state to the d_l-orbital is possible by phosphorescent decay, non-radiative processes and dynamic quenching with the decay rates k_r, k_{nr} and $k_q \cdot c$, respectively. The decay rate of phosphorescent quenching is the product of the bimolecular quenching constant k_q and the quencher concentration c. From Friedl [2013].

4 Setup & Calibration

In this chapter, the wind-wave tank is introduced in section 4.1. The measuring instruments and boundary layer imaging setup are discussed separately in sections 4.2 and 4.3, respectively.

4.1 Annular Wind-Wave Tank

The experiments were carried out at the "Windmühle"[1] of the IUP Heidelberg, a schematic drawing of it is provided in fig. 4.1. The aluminium tank was built roughly 50 years ago at the *Jülich Research Centre*, and first described in detail by Vogt [1976].

Generally speaking, it is made up of two main parts. The bottom part consists of a 10 cm-wide and -deep annular flume mounted on a table-like structure, which is typically filled with water. Its inner diameter is 40 cm and, if filled up completely, the channel holds a volume of approximately 15.7 L. The top part is a cylindrical cover, which can be lifted with the help of a rope and pulley system. It is 33 cm high and 75 cm wide, enclosing a gas volume of about 145.8 L. A wind engine is attached to the inner top part, featuring four rectangularly arranged rotor blades of 35 cm width and 20 cm height. The distance between the bottom structure and the lowest point of the rotor blades is 10 cm. The wind engine is powered by a DC motor, which in turn is regulated by a potentiometer, hence, allowing to regulate the wind speed continuously. The wind-wave tank is equipped with

[1] The small annular wind-wave tank (with relatively large rotor blades) is referred to as "Windmühle".

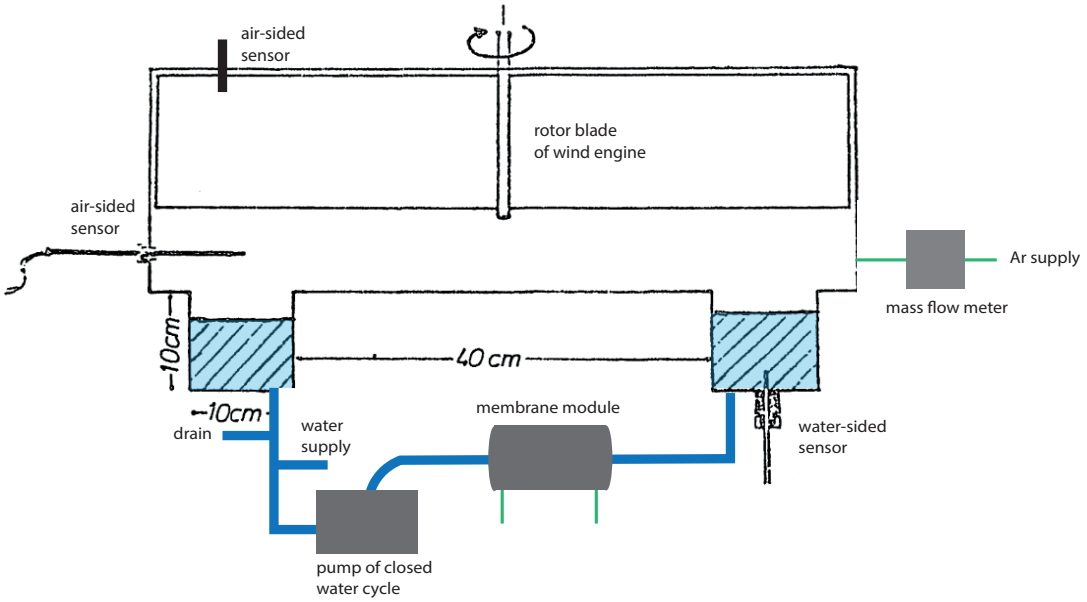

Figure 4.1: Cross-section of the annular wind-wave tank at the IUP Heidelberg. Exemplary locations for adding measuring instruments at the water- and air-side are displayed. The Ar supply and the enclosed water cycle (with water supply pipe and drain) is depicted. Modified from Dutzi [1984].

multiple acrylic windows at the vertical side of the cover to visually monitor the gas exchange experiments. Additionally, at the top, two large anti-glare glass windows (20 cm $\times$ 13 cm) and a small one (15 cm $\times$ 7 cm), all manufactured by *Edmund Optics*, were installed. Together with another glass window at the bottom of the water flume, the light source (top) points directly into the detector (bottom). A detailed description of the boundary layer imaging setup can be found in section 4.3.

The air-side of the tank is flushed with argon (Ar), the flush rate is controlled by an *Analyt-MTC* mass flow meter. The same device also monitors the transfer of oxygen into the deionized water of the flume, which is constantly pumped (*Qingdao Ahead AW500S* pump) through a closed water cycle including a *PermSelect PDMSXA-1.0* membrane gas exchange module. This module is operated in sweep gas mode, and the large membrane surface area of 1 m^2 greatly boosts O_2 uptake of the liquid.

Traditionally, wind-wave tanks have been designed in a linear shape, e.g., the linear channel

of the IUP's *Air-Sea-Interaction* group built by Herzog [2010]. Therefore, it is worth to consider the influence of an annular tank on the experimental outcome, which has been thoroughly discussed by Jähne [1980] and later summarized by Weber [2010]:

- **Infinite fetch.** The fetch length or simply fetch is the distance the wind can blow over water. The longer the fetch at constant wind direction and speed, the larger are the produced waves as wind energy is transferred to the water, until an equilibrium state is reached due to local energy dissipation in the water-side. Therefore, while in linear tanks the size of waves increases towards the downwind end of the channel, the annular-shaped tanks can yield a homogenous wave field (if wind has been constantly applied for sufficient amount of time).

- **Centrifugal force.** The circular geometry alters the typical logarithmic wind profile of linear tanks such that constant wind speeds occur down to the boundary layer. In greater detail, the centrifugal acceleration v^2/r, where v is the tangential velocity and r the distance to the tank's centre, is balanced by a radial pressure gradient $\partial p/\partial r$. Any vertical difference in wind velocity is equalized by the resulting vertical pressure gradient. Ultimately, at the same wind engine speed, this leads to a larger transfer of momentum than compared to a linear tank.

- **Surface films.** These films are made up of substances that decrease the surface tension (energetically favourable), or have a lower density than the surrounding water, and even occur in laboratory experiments, if no counter-measures are taken. Surfactants[2] reduce the size of capillary waves, thus, suppressing the near surface turbulence, which in turn reduces gas transfer rates, as experimentally shown by Schimpf et al. [2006]. Ceniceros [2003] numerically identified an accumulation of surfactants in capillary regions, resulting in (a) net reduction of surface tension and (b) surface tension gradients due to the non-uniform concentration, as the main reasons for weaker capillaries. Hence, particularly in annular wind-wave tanks, surface films falsify gas exchange measurements as the substances indefinitely travel in a circular path on top of the water surface. In linear tanks however, surfactants drift to the downwind end of the channel and thus can be somewhat neglected. In order

[2] **Surf**ace **act**ive **a**ge**nt**s

to tackle the effects of surface films in the experiments presented here, the topmost water layer is repeatedly skimmed and pumped out (*KNF Flodos CH-6210 Sursee* vacuum pump), simultaneously removing any surfactants. Figure 4.2 illustrates the instrument used for this task.

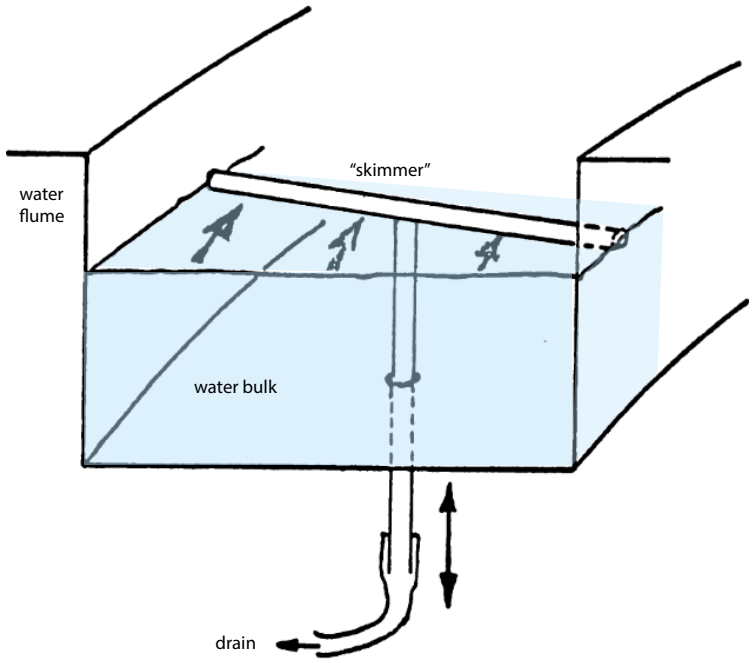

Figure 4.2: The "skimmer" is a T-shaped device, the top part is made up of a vertical drain. It is positioned just below the water surface, which allows pumping out the collected water layer, if slow wind is applied. During experiments, the instrument is lowered to the bottom of the flume and aligned parallel to the water flow in order not to disturb the current. Modified from Dutzi [1984].

4.2 Measuring Instruments

Previously, the "Windmühle" was used for gas exchange experiments of the advanced student laboratory as part of the Heidelberg bachelor curriculum. For this work, the wind-wave tank has been equipped with several (new) measurement devices in order to monitor multiple environmental parameters. In the following, the instruments are introduced by linking them to the respective measurement variable.

4.2.1 Water-Side

- **Speed**. The *Höntzsch ZS30GFE-md20T* anemometer has been fitted to the bottom of the water flume. The rotational speed of the vane is proportional to the fluid's velocity, virtually independent of density, pressure and temperature. The measurement uncertainty is the sum of 1.5 % of reading (RD) and 0.5 % of full scale (FS).

- **Oxygen concentration.** The *OXYBase WR-RS232* oxygen sensor manufactured by *PreSens* measures the percentage of oxygen dissolved in the fluid. The device is two-point calibrated and the measurement uncertainty is extrapolated from these values.

- **Water level.** The *Keller PR-41* static pressure sensor measures the pressure at the bottom of the channel exerted by the water column above it. From the device's output, the static pressure head (i.e., water height) can be computed, or the sensor can be manually calibrated for multiple known water heights. However, if the flow of gas into the atmosphere of the "Windmühle" is changed, the air pressure adjusts accordingly, which in turn alters the pressure readings of the measuring instrument. Therefore, only relative changes of water level (while gas flow is constant) are verifiable.

- **Temperature.** The water temperature is monitored by the *otom PT1000* temperature probe. It is coated in stainless steel to be shielded from the high moisture inside the wind-wave tank. The higher the temperature, the greater the resistance of an internal resistor. The water-side is continuously cooled down with four Peltier coolers attached to the outer bottom part of the water flume. This limits evaporation of water, and prevents condensation, as the water bulk is the coldest surface in contact with the air-side. Formation of water droplets on the inside of the glass window, through which the light source illuminates the water surface, is prevented.

4.2.2 Air-Side

Here, O_2 concentration and temperature are recorded with the same measuring instruments as used on the water-side. Apart from that, the following variables are considered:

- **Wind speed.** This parameter can be derived from two measuring instruments:
  First, the *EM TPL* Prandtl tube combines a basic pitot tube pointing straight into the air flow and a second tube with only holes on the sides, outside any direct air flow. Inside the first component, the moving air is brought to rest as there is no outlet to allow flow to continue. The corresponding pressure is referred to as stagnation pressure. It cannot itself be used to determine flow velocity u. Rather, Bernoulli's equation yields (for an incompressible fluid)

  $$u = \sqrt{\frac{2\,(p_t - p_s)}{\rho}}, \tag{4.1}$$

  where p_t is the stagnation pressure (or total pressure), p_s is the static pressure, which builds up inside the second tube without any holes pointing directly into air flow, and ρ is the air's density. Both tubes are connected to a *TE SM9235* pressure sensor in order to compute the dynamic pressure, i.e., the difference $p_t - p_s$.
  Second, a *VOLTCRAFT* digital laser tachometer can be used to measure the number of revolutions of the wind engine's rotor blades. From there, by taking into account the distance from the centre of the "Windmühle" to the middle of the water flume, the revolutions (in rpm) can be translated to fluid velocity (in $\mathrm{m\,s^{-1}}$) at this particular radius.
  Ultimately, the latter method has been chosen, as the digital output of the pressure sensor was subject to noise at irregular intervals and the density ρ of the atmosphere depends on gas composition, temperature and pressure.

All measuring instruments are connected to a custom-designed printed circuit board, which prepares the signals for processing, and readout with a *Teensy 4.1* microcontroller. Compiled code of a high-level programming language (here, Arduino Programming Language and external libraries) can be stored in the on-chip memory, thus, supporting various data

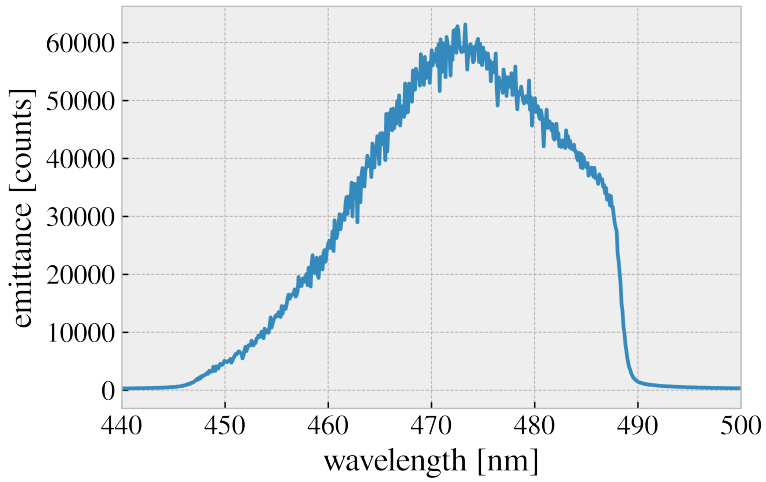

Figure 4.3: Emission spectrum of the light source (blue LEDs and filter) of the final version of the boundary layer imaging setup, recorded with *Ocean Optics USB4000* spectrometer.

communication protocols. The board transfers the environmental parameters to an external computer; for later data analysis, it is advantageous if all variables of an individual measuring interval are linked to a single time stamp.

4.3 Boundary Layer Imaging

Basically, the boundary layer imaging (BLI) setup consists of a light source to excite the Ru complex and a detector to record the water-sided oxygen concentration profiles. The schematics of the final version of the BLI setup are presented at the very end of this section in fig. 4.6.

In greater detail, the Ru complex is excited by the irradiance of eight units of light-emitting diodes (LEDs); always two of them are mounted in a cuboidal passive heat sink, with a length, width and height of 11 cm, 5.4 cm and 6 cm, respectively. The heat sinks are additionally cooled down by two computer fans. A single LED unit is supplied with a voltage of 56 V and current of 300 mA. The light emitted by the LEDs is filtered, ultimately leading

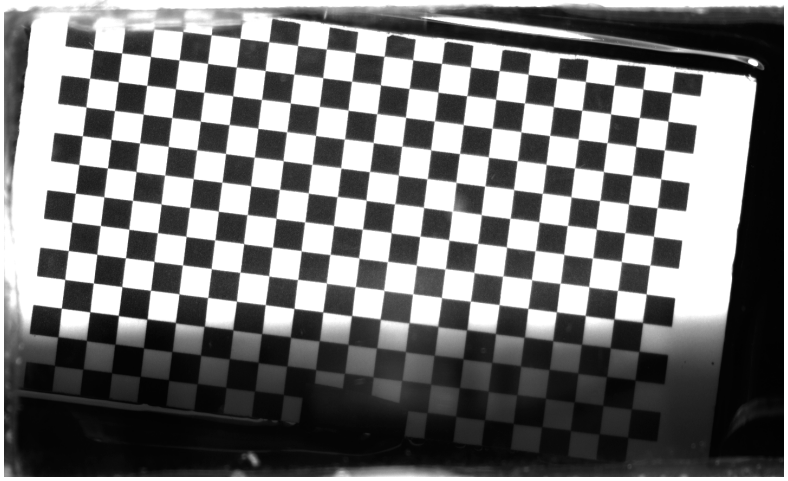

Figure 4.4: Captured height calibration image of the chessboard wood after focussing the camera. An additional light source was placed under the water channel, its shadow is visible in the lower part of the image.

to the emission spectrum shown in fig. 4.3.

The luminescent emission of the excited Ru complex is recorded with a *Basler acA1440-220um* camera, which is equipped with a *Tamron* objective, that has a static focal length of 16 mm. A *TECHSPEC* light red imaging filter, manufactured by *Edmund Optics*, is mounted on the objective. The centre wavelength of transmittance is at 633 nm, with a full width at half maximum (FWHM) of 70 nm, overlapping with the emission spectrum of the Ru complex (see fig. 3.2). The BLI camera is manually focussed on a water height of 8 cm. A chessboard pattern printed on a piece of wood, which is fixed in a way that it floats steadily above the camera on the water surface, facilitates the task. Exemplary, a calibration image is shown in fig. 4.4.
An *USB4000* fibre optic spectrometer coupled to a transmission probe, both devices produced by *Ocean Optics*, can be used to record absorption spectra of the water bulk in order to quantify the concentration of the Ru complex, as discussed in section 5.3. The camera and spectrometer are controlled with the help of heurisko, a programming language specialized for image processing.

Preliminary experiments revealed that the bandpass filters of the LEDs reflect the isotropic luminescent emission of the Ru complex indicator, hence, rendering the gas exchange

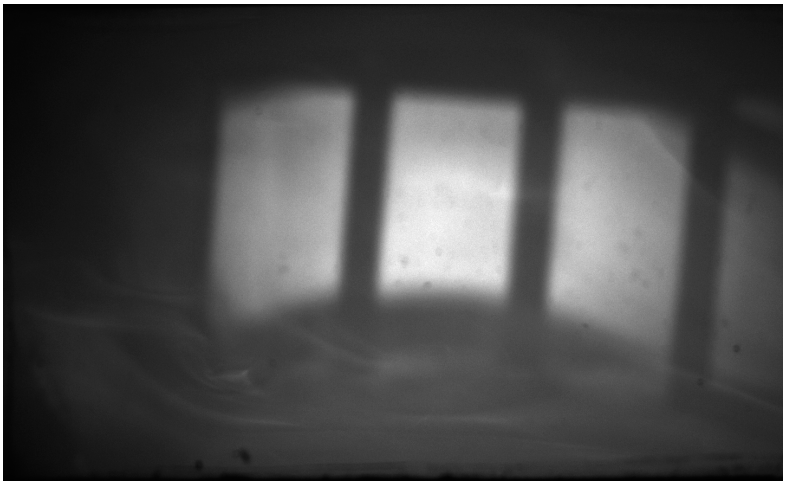

Figure 4.5: Captured image during preliminary BLI experiments. Although structures of the oxygen concentration profile are visible, in particular in the bottom-left corner, the reflection of the LED filters is dominating. The outlines of the pairs of LED units are clearly recognizable.

footprints at the air-water interface virtually invisible (see fig. 4.5). A set of measures has been implemented to reduce the effect of reflection:

- Most importantly, the LED units are mounted on a custom-designed structure, allowing to install the filters at an angle of about 9.6°. Luminescent emission of the indicator in the water bulk, which cannot pass the LED filter, is reflected to the sides of the flume, not in the direction of the camera window at the bottom of the channel.

- Moreover, the inside of the tank's cover is painted black using *BLK3.0* acrylic paint to forestall any reflection effects of the aluminium surface.

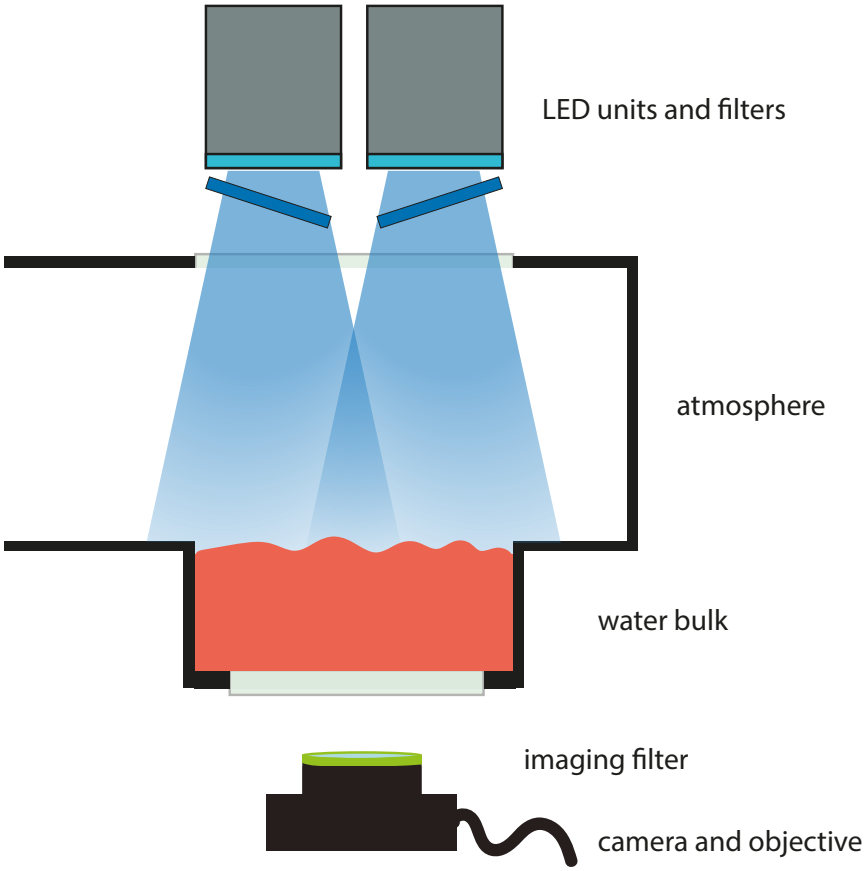

Figure 4.6: Labelled schematic drawing of the complete boundary layer imaging setup.

5 Experiments

This chapter introduces general measurement conditions, followed by an explanation of the experimental procedure and spectral analysis of the Ru complex concentration.

5.1 Conditions

The gas exchange experiments were performed at wind speeds ranging from $2\,\mathrm{m\,s^{-1}}$ to $7\,\mathrm{m\,s^{-1}}$. The water height was approximately 8 cm. All BLI images (of the "systematic" measurements) were acquired with an f-number (aperture value) of 1.4, an exposure time of 2 ms and a frame rate of 100 fps. Additionally, the gain was set to 6 dB, while the remaining camera parameters were not changed from their default values. The camera outputs 8-bit monochrome images with a resolution of 1440 pixels $\times$ 880 pixels. In one cycle, 1024 images are captured and saved as a single TIFF file. In a complete measurement series, five datasets per wind speed were recorded.

5.2 Measurements

In an evasion experiment, the gas transport from the water- to the air-side is investigated. Prior to running experiments, the atmosphere of the wind-wave tank has been flushed with Ar to ensure an O_2-free atmosphere; during the experimental work, 20 SLPM of Ar are continuously added to the air-side. The closed water cycle, pumping water through the

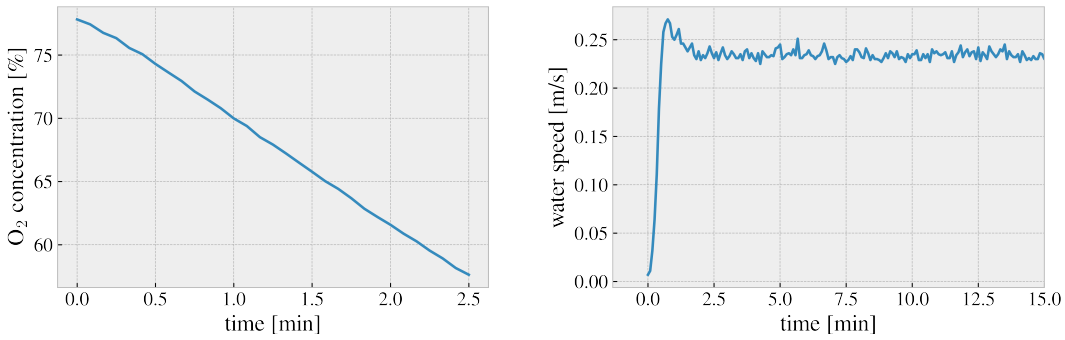

(a) O_2 concentration, air-side

(b) speed of water bulk

Figure 5.1: Time evolution of selected environmental parameters during high-wind-speed experiment ($u = 7\,\mathrm{m\,s^{-1}}$), which starts at $t = 0$. Please note the varying time intervals plotted on the x-axis.

membrane gas exchange module, is turned on until the water reaches an O_2 concentration of roughly 80 %. Applying slow wind aids mixing of O_2-enriched water from the gas exchanger into the water bulk. Next, the "skimmer" is used to remove any surfactants on the water surface. Both processes (oxygenation and skimming) are repeated after having captured all images of a particular wind speed.

The laser tachometer is used to set the engine's rotor blades to the desired wind speed. Then, the LIF images are taken (as explained in section 4.3) and the spectrum of the dissolved Ru complex is recorded. The wind-induced turbulence causes O_2 concentration to drop, while simultaneously building up a constant wave field. In particular, fast winds (and consequently strong waves) decrease the O_2 concentration rapidly, however, the water bulk quickly reaches a steady orbital velocity, as fig. 5.1 illustrates. Therefore, image acquisition can be started right after the wind speed has been adjusted in order not to miss the high O_2 concentration of the water-side.

Measurement series were conducted for three different concentrations of Ru complex.

5.3 Spectroscopy

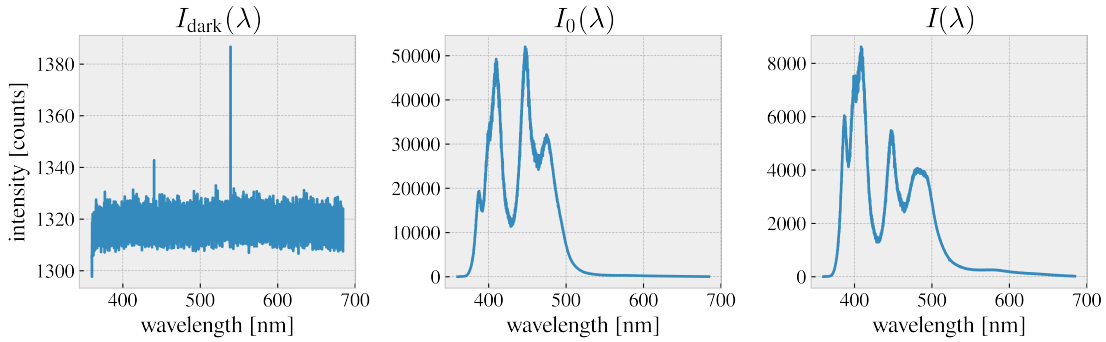

Figure 5.2: Example of a dark spectrum $I_{\text{dark}}(\lambda)$, a lamp spectrum $I_0(\lambda)$ and a measured spectrum I_0 for a concentration of Ru complex of 0.11 mmol L^{-1}. The scaling of the y-axis is adjusted to the respective total number of counts.

The concentration of the Ru complex is monitored with the *Ocean Optics USB4000* spectrometer of the BLI setup, which records intensity spectra. In order to transform intensity spectra into absorption spectra, three different measurements are necessary.

1. The **dark spectrum** $I_{\text{dark}}(\lambda)$ is recorded without any illumination, i.e., by turning off the spectrometer's light source.

2. The **lamp spectrum** $I_0(\lambda)$ refers to the pure spectrum of the light source. Although the tank is filled with ionized water, there is no indicator present.

3. The actual **measured spectrum** I_0 is recorded when the experimental preparation is complete and the selected concentration of Ru complex is dissolved in the water.

For clarity, the individual spectra are plotted in fig. 5.2. Please note that the lamp and the measured spectrum have to be corrected for the baseline offset of the spectrometer, i.e, the dark spectrum is subtracted. The absorption spectrum is computed as

$$A(\lambda) = -\log_{10} \frac{I(\lambda)}{I_0(\lambda)}, \tag{5.1}$$

here, the argument of the logarithm $I(\lambda)/I_0(\lambda)$ is also referred to as the transmission spectrum. The Beer-Lambert law relates the absorbance of an indicator of uniform concentration c to the optical path length l through the fluid, yielding

$$A = \epsilon l c, \tag{5.2}$$

with the molecular attenuation coefficient ϵ. The Ru complex has a coefficient of $\epsilon = (35 \pm 1) \times 10^3\,\mathrm{L\,mol^{-1}\,cm^{-1}}$, if using the decadic logarithm in eq. (5.1), as sometimes the natural logarithm is preferred. The absorption spectra of the different concentrations of Ru complex are presented in fig. 5.3. It is important to note that the indicator concentration c specified in fig. 5.3 is derived from the weight m of the Ru complex, which is added to the water-side prior to experiments, as follows:

$$c = \frac{m \cdot M}{V}, \tag{5.3}$$

where $M = 1853.56\,\mathrm{g\,mol^{-1}}$ is the molecular mass of the Ru complex, and V denotes the water volume of the "Windmühle".
A continuos recording of (absorption) spectra indicates that the concentration of Ru complex does not change significantly throughout a measurement series.

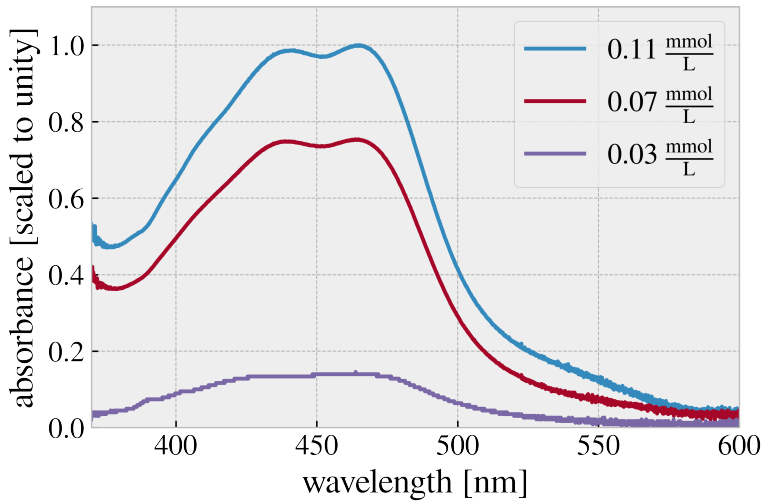

Figure 5.3: Absorption spectra of different concentrations of Ru complex. The maximum absorbance A_{max} of the spectrum with the highest concentration ($0.11\,\text{mmol}\,\text{L}^{-1}$) is determined, and all spectra are scaled with $1/A_{\text{max}}$. According to eq. (5.2), the absorbance is proportional to the concentration of the Ru complex.

6 Results

In this chapter, the recorded oxygen concentration fields are qualitatively discussed, followed by an analysis of the mean image sequence brightness.

6.1 Oxygen Concentration Images

The oxygen quenching BLI method is realized at three different concentrations of Ru complex indicator and multiple wind speeds. The acquired images are enhanced by altering the contrast and brightness, apart from that, no further post-processing is applied. The bright structures arise due to a localized decrease in quencher (oxygen) concentration. Unless otherwise noted, the wind always blows from the right to the left side of the images. The experimental run with the lowest concentration of indicator, namely $0.03\,\mathrm{mmol\,L^{-1}}$, reveals that this is not a sufficient amount of Ru complex dissolved in the water bulk, gas exchange footprints are barely visible, as fig. 6.1 demonstrates. For high wind speeds and a turbulent (wavy) water-side, the irradiance of the LEDs is focussed on wave crests, due to their convex surface. Likewise, the refraction in wave troughs causes the incoming light to diverge, ultimately leading to dark regions in the image. In the following, this phenomenon is referred to as lensing.

If the concentration of Ru complex indicator is increased to $0.07\,\mathrm{mmol\,L^{-1}}$, gas exchange at the air-water interface becomes identifiable. With the onset of waves, bright streaks are prominent in the recorded images, as shown in fig. 6.2. Put together with vertical oxygen concentration profiles (see fig. 6.3), recorded transversely to the wind direction,

Figure 6.1: Oxygen concentration image at low wind speed, $u = 0.4\,\mathrm{m\,s^{-1}}$, and concentration, $c = 0.03\,\mathrm{mmol\,L^{-1}}$. Faint gas exchange footprints are visible at the bottom, the annular bright structure at the top of the image is most-likely a reflection of the tank's cover.

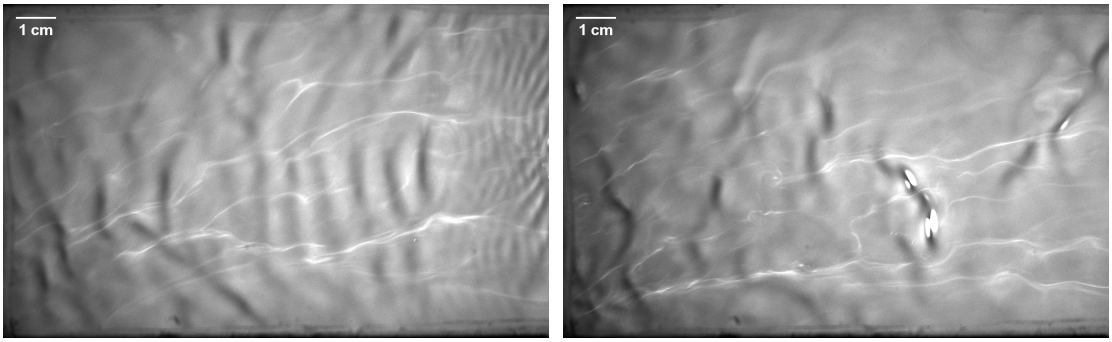

(a) $u = 4\,\mathrm{m\,s^{-1}}$ (b) $u = 4.5\,\mathrm{m\,s^{-1}}$

Figure 6.2: Oxygen concentration images at medium wind speed u and a Ru complex concentration of $c = 0.07\,\mathrm{mmol\,L^{-1}}$. Streaks of low oxygen concentration are clearly visible. With increasing wind speed, the surface waves become bigger, ultimately showing bright structures aligned with the wave crest (b). This phenomenon occurs less frequently for slower wind speeds (a).

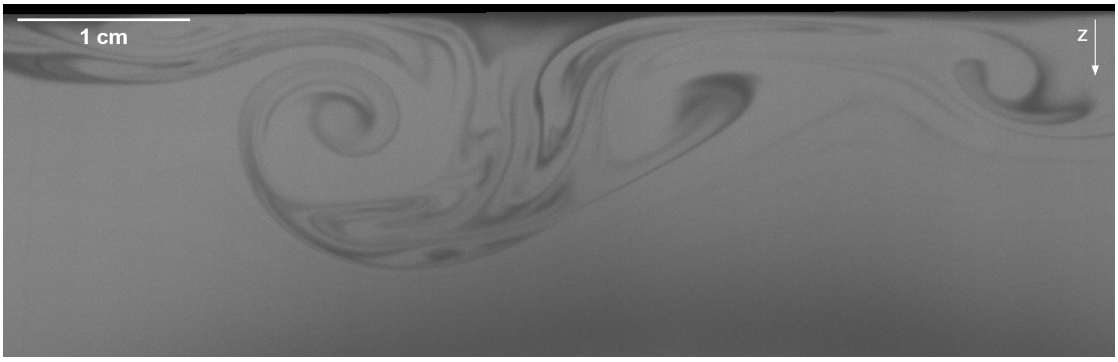

Figure 6.3: Vertical oxygen concentration profile transverse to the wind direction acquired by Arnold [2015]. The oxygen quenching method was utilized in an invasion experiment, thus, leading to a bright water bulk with low oxygen concentration. The downward-facing, oxygen-enriched flow clearly forms vortices, their rotational axes are parallel to the wind direction. Consequently, bright, oxygen-free water is moved from the water bulk to the surface (in particular on the right side of the image).

it is most likely that the underlying mechanism of the streak formation is similar to the driving process of Langmuir circulations, introduced in section 2.2.2.

The third experimental run has been executed with a Ru complex indicator concentration of $0.11\,\mathrm{mmol\,L^{-1}}$. Generally speaking, the streak pattern is already visible at low wind speeds and is more prominent than compared to previous concentrations of Ru complex. At high wind speeds, the oxygen footprints are virtually impossible to detect; on the one hand, due to lensing, on the other hand, due to the reduced mass boundary layer thickness, as turbulence increases. The images in fig. 6.4 show the effects of wind speed on the oxygen concentration profiles at the air-water interface.

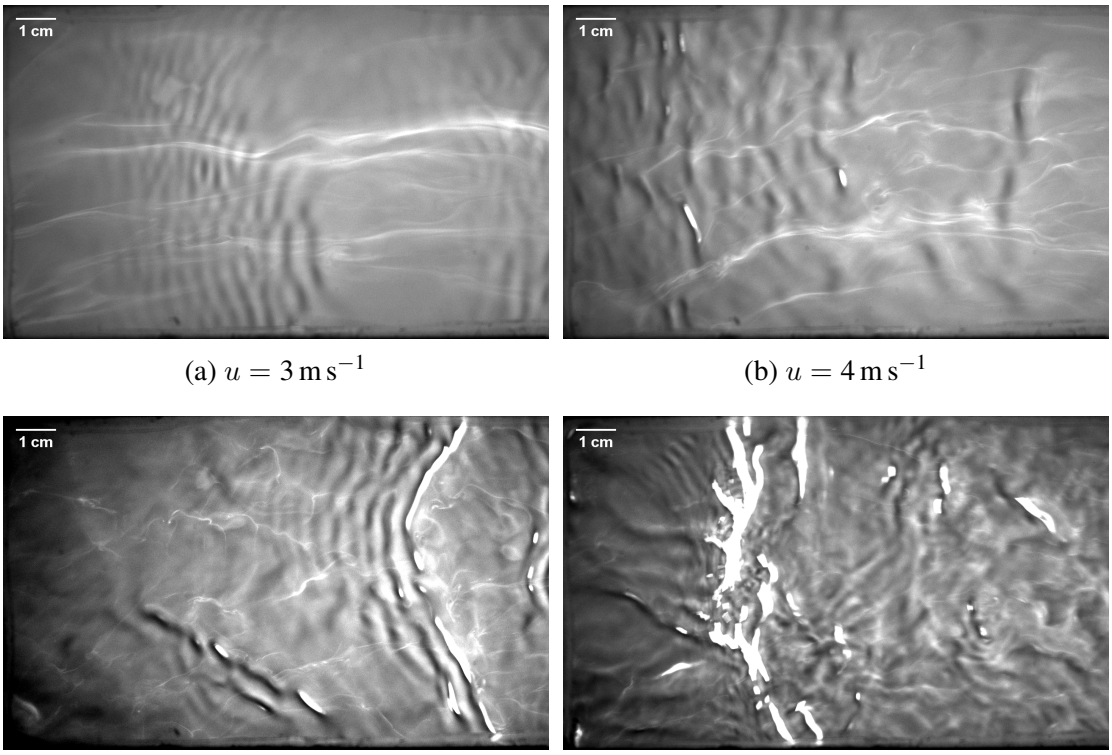

(a) $u = 3\,\mathrm{m\,s^{-1}}$ (b) $u = 4\,\mathrm{m\,s^{-1}}$

(c) $u = 6\,\mathrm{m\,s^{-1}}$ (d) $u = 7\,\mathrm{m\,s^{-1}}$

Figure 6.4: Oxygen concentration image series for multiple wind speeds u and a high Ru complex concentration of $c = 0.11\,\mathrm{mmol\,L^{-1}}$.

6.2 Mean Greyscale Brightness

The recorded images are 8-bit greyscale encoded, meaning that the value of each pixel represents an amount of light, i.e., it carries only intensity information. The pixel values range from 0 (black) to 256 (white). When applying the oxygen quenching method in an evasion experiment, the mean greyscale value of an image stack (in this study, a series of 1024 individual images) should—theoretically—decrease with increasing wind speed, as the size of the mass boundary layer decreases when turbulent flow intensifies.

Figure 6.5a reveals that the greater the wind speed, the higher is the mean greyscale of an entire measurement series. Here, a measurement series refers to all the image sequences recorded at the same wind speed. The increase of greyscale pixel value is mainly due to the quick diffusion of the quencher into the atmosphere of the "Windmühle". During a measurement series of fast wind speed, the oxygen concentration drops quickly (see fig. 5.1a), thus, the Ru complex emits more luminescent radiation towards the end of the measurement series, increasing the size of the error bands. However, if just plotting the first recorded image sequence of a measurement series, as in fig. 6.5b, the increase of greyscale pixel value with increasing wind speed persists, most-likely due to the bright reflection patterns along wave crests of large surface waves (e.g., see fig. 6.4d). Both mechanisms interfere with the theoretically predicted decrease of mean greyscale value for a smaller mass boundary layer thickness.

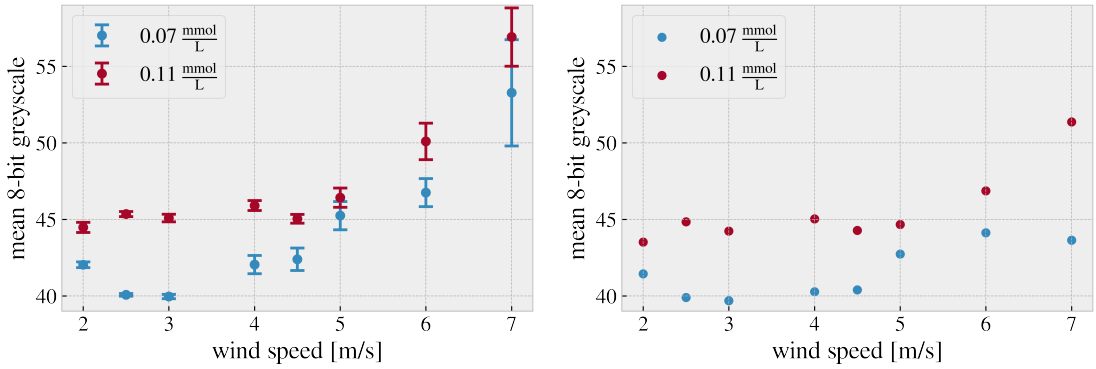

Figure 6.5: The mean greyscale pixel value in respect to the applied wind speed for two different concentrations of Ru complex is plotted. The mean greyscale of an individual image sequence is computed, and either averaged with the results of the other image sequences of the same measurement series (a), or the mean greyscale of the first recorded image stack is used (b). In (a), the error band refers to the error of the mean, when averaging the mean greyscale of multiple image stacks. In (b), when averaging just a single image stack, the size of error bands bears no meaningful context. The computation has been performed on unedited, raw TIFF files, all recorded with the same exposure time of 2 ms.

7 Conclusion & Outlook

The oxygen quenching method has been successfully implemented and recorded images were qualitatively discussed. On top, a quantitative analysis of the mean greyscale brightness of an image sequences was performed, although the raw data acquired can be investigated in greater depth. The "Windmühle" has been mounted with multiple modern measuring devices, at the water- as well as air-side, and is ready to be used for further small-scale gas exchange experiments. The BLI setup works as expected, however, the acquired images are still showing minor reflection patterns, in particular at wave crests under high wind speeds ($u > 5\,\mathrm{m\,s^{-1}}$).

Systematic measurements of the water-sided oxygen concentration fields can be performed, optionally, at a larger wind-wave tank. The quenching method can also be combined with the pH method (see section 3.1), leading to an oxygen evasion and acidic gas invasion experiment.

Bibliography

Arnold, N. “Visualisierung des Gasaustauschs an der windbewegten Wasseroberfläche mittels vertikaler Konzentrationsfelder von gelöstem Sauerstoff quer zur Windrichtung.” Bachelor’s thesis. Institut für Umweltphysik, Universität Heidelberg, Germany, 2015. DOI: 10.11588/heidok.00018411.

Castellano, F. N. and J. R. Lakowicz. “A water-soluble luminescence oxygen sensor.” In: *Photochemistry and Photobiology* 67.2 (1998), pp. 179–183. DOI: 10.1111/j.1751-1097.1998.tb05184.x.

Ceniceros, H. D. “The effects of surfactants on the formation and evolution of capillary waves.” In: *Physics of Fluids* 15.1 (2003), pp. 245–256. DOI: 10.1063/1.1528940.

Dutzi, A. „Untersuchungen zum Einfluss der Temperatur auf den Gasaustausch“. Diplomarbeit. IUP D-190: Institut für Umweltphysik, Fakultät für Physik und Astronomie, Univ. Heidelberg, 1984. DOI: 10.5281/zenodo.14919.

Fick, A. „Ueber Diffusion“. In: *Annalen der Physik* 170.1 (1855), S. 59–86. DOI: 10.1002/andp.18551700105.

Friedl, F. “Investigating the Transfer of Oxygen at the Wavy Air-Water Interface under Wind-Induced Turbulence.” Dissertation. Institut für Umweltphysik, Fakultät für Physik und Astronomie, Univ. Heidelberg, 2013. DOI: 10.11588/heidok.00014582.

Herzog, A. “Imaging of Water-sided Gas-Concentration Fields at a Wind-Driven, Wavy Air-Water Interface.” Dissertation. Institut für Umweltphysik, Fakultät für Physik und Astronomie, Univ. Heidelberg, 2010. DOI: 10.11588/heidok.00011220.

Hinze, J. O. *Turbulence*. 2nd. McGraw-Hill series in mechanical engineering. New York: McGraw-Hill, 1975.

IPCC. “Summary for policymakers.” In: *Climate Change 2013: The Physical Science Basis. Contribution of Working Group I to the Fifth Assessment Report of the Intergovernmen-*

tal Panel on Climate Change. Ed. by T. F. Stocker et al. Cambridge, UK: Cambridge University Press, 2013, pp. 3–29. DOI: 10.1017/CBO9781107415324.004.

Jähne, B. „Zur Parametrisierung des Gasaustauschs mit Hilfe von Laborexperimenten“. Dissertation. IUP D-145: Institut für Umweltphysik, 1980. DOI: 10.11588/heidok.00016796.

Jähne, B. et al. “On the parameters influencing air-water gas exchange.” In: *Journal of Geophysical Research* 92 (1987), pp. 1937–1950. DOI: 10.1029/JC092iC02p01937.

Kräuter, C. “Visualization of air-water gas exchange.” Dissertation. Institut für Umweltphysik, Fakultät für Physik und Astronomie, Univ. Heidelberg, 2015. DOI: 10.11588/heidok.00018209.

Lakowicz, J. R. *Principles of Fluorescence Spectroscopy*. 3rd ed. Springer US, 2006. DOI: 10.1007/978-0-387-46312-4.

Langmuir. “Surface motion of water induced by wind.” In: *Science* 87 (1938), pp. 119–124. DOI: 10.1126/science.87.2250.119.

Roedel, W. and T. Wagner. *Physik unserer Umwelt: Die Atmosphäre*. Springer, 2011. ISBN: 9783642157288.

Schimpf, U. et al. “Infrared imaging: a novel tool to investigate the influence of surface slicks on air-sea gas transfer.” In: *Marine Surface Films: Chemical Characteristics, Influence on Air-Sea Interactions, and Remote Sensing*. Ed. by M. Gade et al. Springer, 2006, pp. 239–252. DOI: 10.1007/3-540-33271-5_21.

Stokes, G. G. “On the Effect of the Internal Friction of Fluids on the Motion of Pendulums.” In: Cambridge University Press, 1850. DOI: 10.1017/cbo9780511702266.002.

Veron, F. and W. K. Melville. “Experiments on the stability and transition of wind-driven water surfaces.” In: *Journal of Fluid Mechanics* 446 (2001), pp. 25–65. DOI: 10.1017/S0022112001005638.

Vogt, H. J. „Isotopentrennung bei der Verdampfung von Wasser“. Deutsch. Dissertation. Univ. Heidelberg, 1976.

Weber, R. “Setup of a Laser Slope Gauge for the Measurement of Wave Slope Distributions at the Small Circular Wind Wave Facility.” Bachelor thesis. Institut für Umweltphysik, Fakultät für Physik und Astronomie, Univ. Heidelberg, 2010.

Wolff, L. M. et al. “A fluorescence technique to measure concentration gradients near an interface.” In: *Air-Water Mass Transfer, selected papers from the 2nd Int. Symposium on*

Gas Transfer at Water Surfaces. Ed. by S. C. Wilhelms and J. S. Gulliver. Minneapolis: ASCE, 1991, pp. 210–218.